Supporting Information

The semiquinone at the Q_i-site of the bc_1 complex explored using HYSCORE spectroscopy and specific isotopic labeling of ubiquinone in *Rhodobacter sphaeroides* via ^{13}C methionine and construction of a methionine auxotroph

Sangjin Hong,[§] Wagner de Almeida,[&] Alexander T. Taguchi,[¶] Rimma I. Samoilova,[Δ] Robert B. Gennis,[§] Patrick J. O'Malley,[&] Sergei A. Dikanov,[‡] and Antony R. Crofts*[,§]

[§]*Department of Biochemistry, University of Illinois at Urbana-Champaign, Urbana, Illinois 61801, United States*

[&]*School of Chemistry, The University of Manchester, Manchester M13 9PL, U.K.*

[¶]*Center for Biophysics and Computational Biology, University of Illinois at Urbana-Champaign, Urbana, Illinois 61801, United States*

[Δ]*Voevodsky Institute of Chemical Kinetics & Combustions, Russian Academy of Sciences, Novosibirsk 630090, Russian Federation*

[‡]*Department of Veterinary Clinical Medicine, University of Illinois at Urbana-Champaign, Urbana, Illinois 61801, United States*

Antimycin-sensitive SQ. The generation of SQ at the Q_i-site is inhibited by antimycin A, an inhibitor specific to the site. In the presence of antimycin, an antimycin-insensitive signal with similar line-shape but much lower amplitude was observed, the nature of which has not been characterized. In Fig. S1, the EPR spectra generated in the absence and presence of antimycin are shown for the preparation used for characterization of the antimycin-sensitive SQ species. Double-integration of the CW-spectra was used to quantify the relative occupancy. The spectra were obtained under conditions for maximal occupancy of SQ, the top of the bell-shaped curve in Fig. 2 of the main text, which shows the relative occupancy determined from the difference between the traces in the absence and presence of antimycin. In contrast to the well-defined bell-shaped curve characteristic of SQ species, the amplitude of the antimycin-insensitive component was (within the accuracy of measurement) constant over the range of the titration.

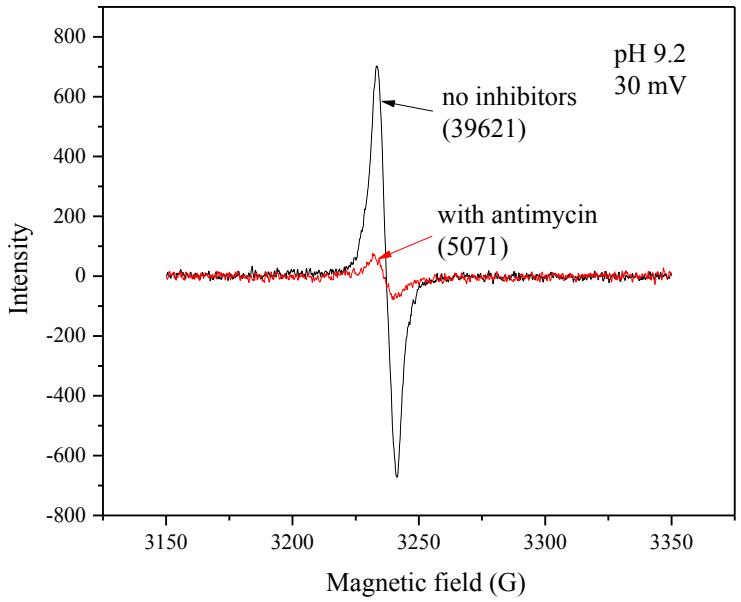

Figure S1. Quantification of the CW-EPR spectra obtained in the absence and presence of antimycin. Spectra obtained at the maximum of the titration curve for the antimycin sensitive component. Conditions were as in Fig. 2 of the text. The numbers in parentheses show values obtained by successive integration of the signal over the range 3225 to 3250 G, demonstrating that 87% of the signal in the absence of antimycin was sensitive to addition of antimycin. Integration was accomplished using the feature available in the OriginPro 9 software package (Origin Lab Corporation, Northampton, MA 01060, USA).

Powder ^{13}C ESEEM spectra. The high-resolution pulsed EPR techniques, such as ESEEM and ENDOR, make use of the paramagnetic properties of the SQ intermediate, its interactions with nearby magnetic nuclei of the protein, the aqueous solvent, and the quinone molecule itself. 1D and 2D ESEEM, can be used to explore the fine-tuning of the environment, and the geometry of substituents and electronic structure of the SQ, via the isotropic and anisotropic hyperfine interactions with magnetic nuclei (^{13}C in this work).[1] ESEEM measures frequencies of nuclear transitions from nuclei interacting with an S=1/2 electron spin of the SQ. There are only two transitions with frequencies ν_α and ν_β for ^{13}C with nuclear spin I=1/2, corresponding to two different states $m_s=\pm1/2$ of the SQ electron spin in a constant applied magnetic field. The value of the frequencies depends on the vector sum of the applied magnetic field and local magnetic field induced at the nucleus by the isotropic and anisotropic hyperfine interactions with the electron spin. In this work we used X-band EPR with microwave frequency ~9.7 GHz and magnetic field ~350 mT. The X-band EPR

spectrum of the SQ in frozen solutions is a single line with the width ~0.8-1.0 mT with unresolved hyperfine structure. This width is comparable to the excitation width of the EPR spectrum by microwave pulses. In this case, the pulses can be considered as a giving a complete excitation of the powder EPR spectrum and thus the ESEEM spectra obtained are the powder-type spectra of nuclear frequencies with all different orientations of applied magnetic field relative to the principal axes of ^{13}C hyperfine tensor(s). The frequencies of ν_α and ν_β transitions vary between

$$\nu_{\alpha(\beta)\perp} = |\nu_C + (-) A_\perp/2| \quad \text{and}$$
$$\nu_{\alpha(\beta)\parallel} = |\nu_C + (-) A_\parallel/2| \qquad (1)$$

corresponding to the perpendicular and parallel orientations of the magnetic field and the unique axis of the axial hyperfine tensor (ν_C is the Zeeman frequency of ^{13}C in the applied magnetic field, $A_\perp = |a - T|$ and $A_\parallel = |a + 2T|$, a is the isotropic hyperfine constant, and the T-components of the anisotropic hyperfine tensor are ($-T$, $-T$, $2T$). The principal values of the rhombic hyperfine tensor can be defined as follows: $(-T(1 + \delta), -T(1 - \delta), 2T)$ with $0 \leq \delta \leq 1$, where δ is a rhombic parameter.

In this work we used HYSCORE because it provides better resolution of the extended lines of low intensity. The HYSCORE experiment creates off-diagonal cross-peaks (ν_α, ν_β) and (ν_β, ν_α) from each I=1/2 nucleus in the 2D spectrum. Powder HYSCORE spectra of I = ½ nuclei reveal, in the form of cross-ridges, the interdependence of ν_α and ν_β in the same orientations (see Figure 1). The two coordinates of the arbitrary point at the cross-ridge, described in the first-order by the equation

$$\nu_{\alpha(\beta)} = |\nu_c + (-) A/2| \qquad (2)$$

can be used for the first-order estimate of the corresponding hyperfine coupling constant A:

$$\nu_\alpha - \nu_\beta = A \qquad (3)$$

Analysis of the ridges in $(\nu_\alpha)^2$ *vs*. $(\nu_\beta)^2$ coordinates allows for direct, simultaneous determination of the isotropic a and anisotropic T components of the hyperfine tensor as described below.[2]

Analysis of ^{13}C cross-peaks. An analytical estimate of the ^{13}C hyperfine tensors, i.e. a (isotropic coupling constant) and T (anisotropic coupling constant) was performed by plotting the HYSCORE spectrum in $(\nu_1)^2$ *vs*. $(\nu_2)^2$ coordinates. By doing so, cross-peaks that are approximately axial appear as linear segments that can be fit to a linear regression. Intersection points of the linear fit with the line $|\nu_1 \pm \nu_2| = 2\nu_C$ define the principal values of the hyperfine tensor.[1,2] There are two possible assignments to ($\nu_{\alpha\perp}$, $\nu_{\beta\perp}$) or ($\nu_{\alpha\parallel}$, $\nu_{\beta\parallel}$) for each crossing point and, consequently, two solutions, one for each assignment. The tensors obtained from the analysis of the SQ_i spectra are summarized in Table S1. Uncertainty in

assignment of ν_1 to ν_α or ν_β and, respectively, ν_2 to ν_β or ν_α, allows alternate signs of a and T in both solutions.

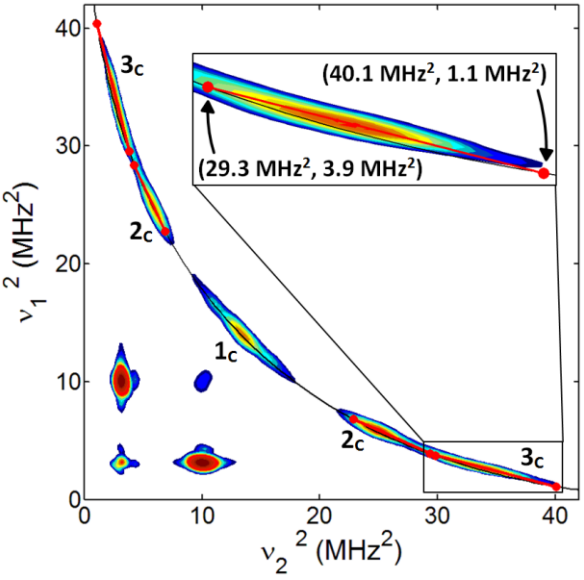

Figure S2. Contour presentation of the HYSCORE spectra of SQ_i (Figure 3) in $((\nu_1)^2$ *vs.* $(\nu_2)^2)$ coordinates. The black curve is defined by $|\nu_1 + \nu_2| = 2\nu_C$. The insert shows the linear regression fit for cross-peak $\mathbf{3_C}$ in greater detail.

Table S1. The ^{13}C hyperfine tensors determined from the parameters of linear regression fits of the cross-peaks.

Site	Set	Intersection (MHz^2)	($\nu_{\alpha\perp}$,$\nu_{\beta\perp}$), MHz	($\nu_{\alpha\parallel}$,$\nu_{\beta\parallel}$), MHz	(a, T), MHz
Q_A[a]	$\mathbf{2_C}$	(22.6 ± 1.5, 6.9 ± 0.8)	(4.2, 3.2)	(4.8, 2.6)	(1.3 ± 0.2, 0.4 ± 0.1)
		(17.2 ± 0.4, 10.5 ± 0.3)	(4.8, 2.6)	(4.2, 3.2)	(-1.7 ± 0.2, 0.4 ± 0.1)
	$\mathbf{3_C}$	(32.8 ± 0.2, 2.8 ± 0.1)	(5.1, 2.3)	(5.7, 1.8)	(3.2 ± 0.1, 0.4 ± 0.1)
		(26.2 ± 1.0, 5.2 ± 0.4)	(5.7, 1.7)	(5.1, 2.3)	(-3.6 ± 0.1, 0.4 ± 0.1)
Q_B[a]	$\mathbf{1_C}$	(23.7 ± 0.8, 6.4 ± 0.4)	(4.2, 3.2)	(4.9, 2.5)	(1.4 ± 0.2, 0.5 ± 0.1)
		(17.3 ± 0.7, 10.4 ± 0.6)	(4.9, 2.5)	(4.2, 3.2)	(-1.9 ± 0.2, 0.5 ± 0.1)
	$\mathbf{2_C}$	(35.0 ± 0.3, 2.2 ± 0.1)	(5.3, 2.1)	(5.9, 1.5)	(3.6 ± 0.1, 0.4 ± 0.1)
		(28.3 ± 0.9, 4.3 ± 0.4)	(5.9, 1.5)	(5.3, 2.1)	(-4.0 ± 0.1, 0.4 ± 0.1)
	$\mathbf{3_C}$	(43.2 ± 0.3, 0.7 ± 0.1)	(5.7, 1.7)	(6.6, 0.8)	(4.6 ± 0.1, 0.6 ± 0.1)
		(32.7 ± 0.6, 2.8 ± 0.2)	(6.6, 0.8)	(5.7, 1.7)	(-5.2 ± 0.1, 0.6 ± 0.1)
Q_i	$\mathbf{2_C}$	(29.1 ± 1.5, 4.0 ± 0.5)	(5.4, 2.0)	(4.8, 2.6)	(2.6 ± 0.1, 0.4± 0.1)
		(22.8 ± 0.1, 6.8 ± 0.1)	(4.8, 2.6)	(5.4, 2.0)	(-3.0 ± 0.2, 0.4 ± 0.1)
	$\mathbf{3_C}$	(40.2 ± 0.3, 1.1 ± 0.1)	(6.3, 1.0)	(5.4, 2.0)	(4.1 ± 0.1, 0.6 ± 0.1)
		(29.4 ± 0.2, 3.8 ± 0.1)	(5.4, 2.0)	(6.3, 1.0)	(-4.7 ± 0.1, 0.6 ± 0.1)

[a]from ref. 3

Table S2. ^{13}C hyperfine tensors determined from the spectral simulations.

Site	Set	*a* (MHz)	*T* (MHz)	Peak Max[a]	Peak Max[b]
Q_A[c]	$\mathbf{1_C}$	0	0.4	(3.7,3.7)	(3.7, 3.7)
	$\mathbf{2_C}$	1.3	0.5	(4.3,3.1)	(4.3, 3.1)
		-1.7	0.4	(4.5,2.9)	
	$\mathbf{3_C}$	3.2	0.4	(5.3,2.1)	(5.5, 1.9)
		-3.6	0.4	(5.5,1.9)	
Q_B[c]	$\mathbf{1_C}$	1.5	0.4 (δ=0.8)	(4.5,2.9)	(4.5, 3.0)
		1.4	0.5	(4.3,3.1)	
		-1.9	0.5	(4.6,2.7)	
	$\mathbf{2_C}$	-3.9	0.4	(5.6,1.8)	(5.7 ,1.7)
		3.6	0.4	(5.5, 1.9)	
		-4.0	0.4	(5.8,1.6)	
	$\mathbf{3_C}$	4.7	0.4 (δ=0.3)	(6.0,1.4)	(6.0, 1.5)
		4.6	0.6	(5.8,1.6)	
		-5.2	0.6	(6.2,1.2)	
Q_i	$\mathbf{1_C}$	0.2 (60%) & 1.1 (40%)	0.5 (δ=0.4)	(3.7, 3.7)	(3.7, 3.7)
	$\mathbf{2_C}$	2.5	0.5 (δ=0.4)	(5.0, 2.4)	(5.0, 2.4)
	$\mathbf{3_C}$	-4.4	0.6 (δ=0.3)	(5.8, 1.6)	(5.8, 1.6)

[a] Peak Maximum from simulation; [b] Peak Maximum from experimental data; [c]from ref. 3.

Simulated spectra

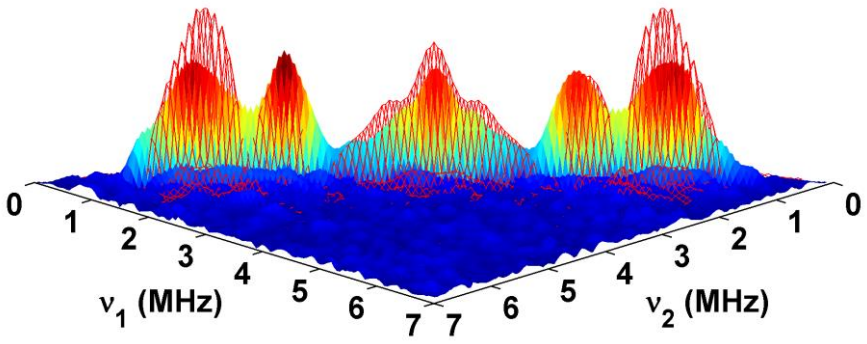

Figure S3 (A). The ^{13}C-Q_i spectrum was simulated with the same sign solution axial tensors from the squared-frequency analysis for $\mathbf{2_C}$ and $\mathbf{3_C}$. Simulation parameters: [a_1 = 0.2 (60%) & 1.1 (40%), T_1 = 0.5, δ = 0.4], [a_2 = 2.6, T_2 = 0.4], [a_3 = 4.1, T_3 = 0.6] MHz.

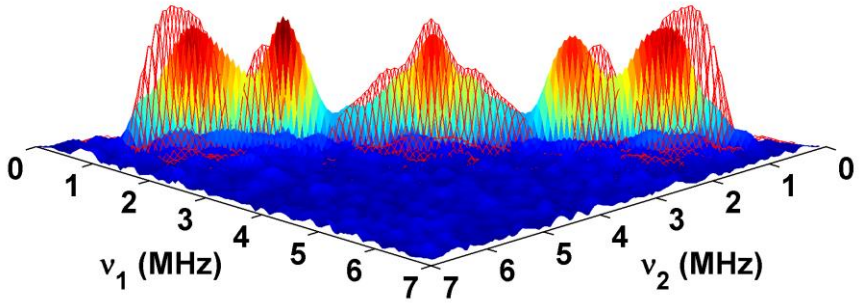

Figure S3 (B). The ^{13}C-Q_i spectrum was simulated with the opposite sign solution axial tensors from the squared-frequency analysis for $\mathbf{2_C}$ and $\mathbf{3_C}$. Simulation parameters: [a_1 = 0.2 (60%) & 1.1 (40%), T_1 = 0.5, δ = 0.4], [a_2 = -3.0, T_2 = 0.4], [a_3 = -4.7, T_3 = 0.6] MHz.

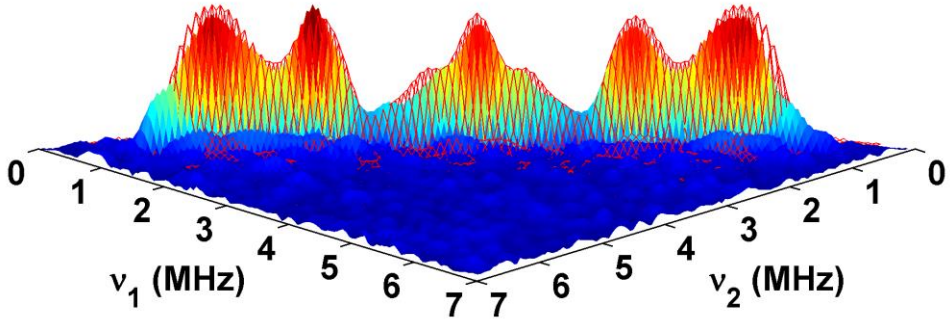

Figure S3 (C). The ^{13}C-Q_i spectrum was simulated with the rhombic tensors. Simulation parameters: [a_1 = 0.2 (60%) & 1.1 (40%), T_1 = 0.5, δ = 0.4], [a_2 = 2.5, T_2 = 0.5, δ = 0.4], [a_3 = -4.4, T_3 = 0.6, δ = 0.3] MHz.

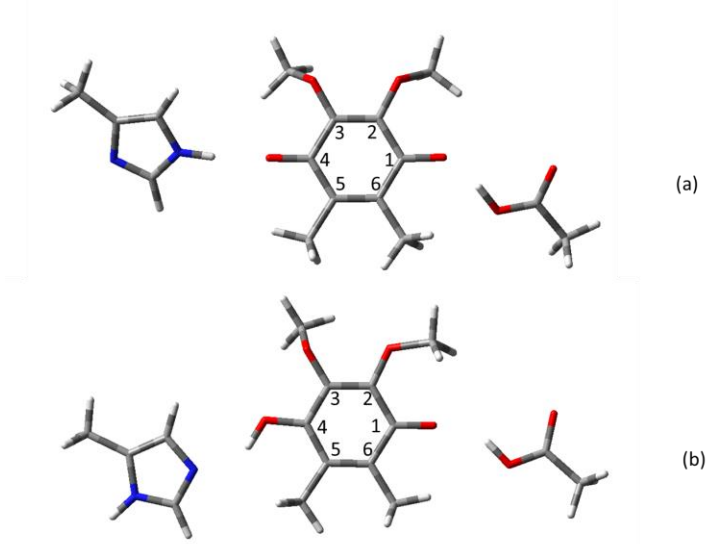

Figure S4. Optimised models of SQ in the Q_i active site for deprotonated H201 N_δ (top) and protonated H201 N_δ (bottom). Starting geometry used was taken from chain C of the 1PP9.pdb file.

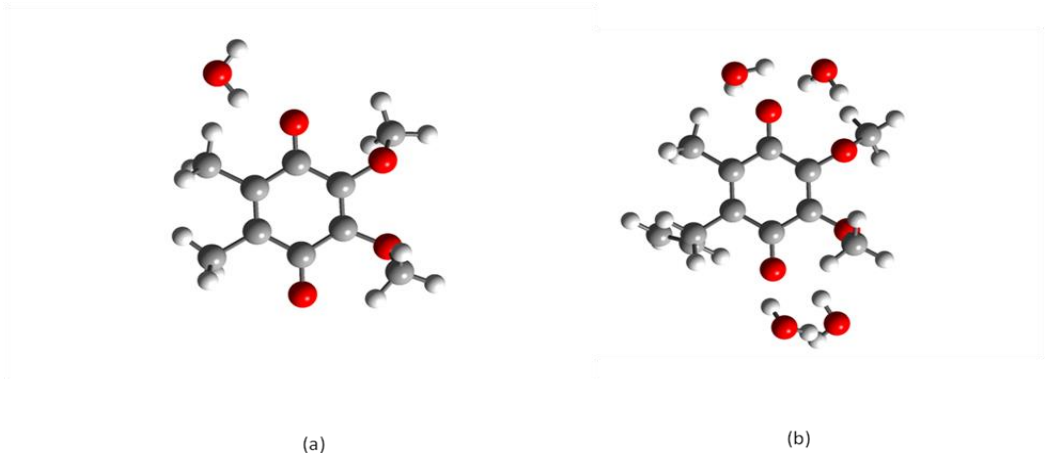

Figure S5. Models used for (a) SQ_{M2} and (b) SQ_{M1}.

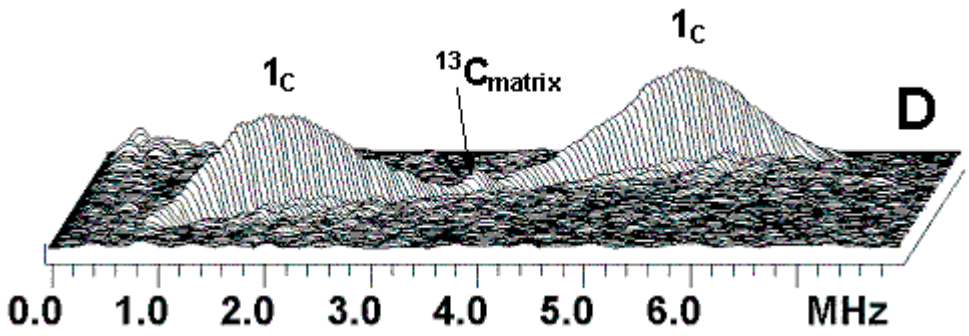

Figure S6. Stacked (D) presentations of the HYSCORE spectrum of the UQ-8 anion-radical with ^{13}C labeled methyl and methoxy groups in frozen isopropanol solution (magnetic field 345.1 mT, time between first and second pulses τ=136 ns, microwave frequency 9.682 GHz (isopropanol)). From ref.4.

References.

1. Dikanov, S. A. (2013) Resolving protein-semiquinone interactions by two-dimensional ESEEM spectroscopy. *Electron Paramagn. Resonan. 23*, 103−179.

2. Dikanov, S. A., and Bowman, M. K. (1995) Cross-peak lineshape of two-dimensional ESEEM spectra in disordered S=1/2, I=1/2 spin system. *J. Magn. Reson., Ser. A 116*, 125−128.
3. Taguchi, A. T., O'Malley, P. J., Wraight, C. A., and Dikanov, S. A. (2013) Conformational differences between the methoxy groups of Q_A and Q_B site ubisemiquinones in bacterial reaction centers: A key role for methoxy group orientation in modulating ubiquinone redox potential. *Biochemistry 52*, 4648-4655.
4. Lin, M. T., Shubin, A. A., Samoilova, R. I., Narasimhulu, K. V., Baldansuren, A., Gennis, R. B., and Dikanov, S. A. (2011) Exploring by pulsed EPR the electronic structure of ubisemiquinone bound at the Q_H site of cytochrome *bo*$_3$ from *Escherichia coli* with *in vivo* ^{13}C-labeled methyl and methoxy substituents. *J. Biol. Chem. 286*, 10105-10114.